High-mobility compensated semimetals, orbital magnetization and umklapp scattering in bilayer graphene moiré superlattices

Artur L. Shilov,[1] Mikhail A. Kashchenko,[2] Pierre A. Pantaleón Peralta,[3] Yibo Wang,[4] Mikhail Kravtsov,[1,4] Andrei Kudriashov,[1,4] Zhen Zhan,[3] Takashi Taniguchi,[5] Kenji Watanabe,[6] Sergey Slizovskiy,[7] Kostya S. Novoselov,[4] Vladimir I. Fal'ko,[7] Francisco Guinea,[3,8] and Denis A. Bandurin*[,1]

[1] *Department of Materials Science and Engineering, National University of Singapore, Singapore, 117575, Singapore*

[2] *Programmable Functional Materials Lab, Center for Neurophysics and Neuromorphic Technologies, Moscow, 127495, Russia*

[3] *IMDEA Nanoscience, Faraday 9, Madrid, 28015, Spain*

[4] *Institute for Functional Intelligent Materials, National University of Singapore, Singapore, 117575, Singapore*

[5] *International Center for Materials Nanoarchitectonics, National Institute of Material Science, Tsukuba, 305-0044, Japan*

[6] *Research Center for Functional Materials, National Institute of Material Science, Tsukuba, 305-0044, Japan*

[7] *School of Physics and Astronomy, University of Manchester, Manchester, M13 9PL, UK*

[8] *Donostia International Physics Center, Paseo Manuel de Lardizábal 4, San Sebastián, 20018, Spain*

* E-mail: dab@nus.edu.sg

Abstract

Twist-controlled moiré superlattices (MS) have emerged as a versatile platform for realizing artificial systems with complex electronic spectra. The combination of Bernal-stacked bilayer graphene (BLG) and hexagonal boron nitride (hBN) can give rise to an interesting MS, that has recently featured a set of unexpected behaviors, such as unconventional ferroelectricity and the electronic ratchet effect. Yet, the understanding of the electronic properties of BLG/hBN MS has, at present, remained fairly limited. Here, we combine magneto-transport and low-energy sub-THz excitation to gain insights into the properties of this MS. We demonstrate that the alignment between BLG and hBN crystal lattices results in the emergence of compensated semimetals at some integer fillings of the moiré bands, separated by van Hove singularities where Lifshitz transition occurs. A particularly pronounced semimetal develops when eight holes reside in the moiré unit cell, where coexisting high-mobility electron and hole systems feature strong magnetoresistance reaching 2350% already at $B = 0.25$ T. Next, by measuring the THz-driven Nernst effect in remote bands, we observe valley splitting, indicating an orbital magnetization characterized by a strongly enhanced effective g_{v}-factor of 340. Finally, using THz photoresistance measurements, we show that the high-temperature conductivity of the BLG/hBN MS is limited by electron-electron umklapp processes. Our multi-faceted analysis introduces THz-driven magnetotransport as a convenient tool to probe the band structure and interaction effects in van der Waals materials and provides a comprehensive understanding of the BLG/hBN MS.

KEYWORDS: Moiré superlattices, bilayer graphene, orbital magnetization, compensated semimetals, umklapp scattering, terahertz.

When atomically flat low-dimensional materials are brought into van der Waals (vdW) proximity with one another, they form a long-wavelength moiré superlattice if their crystal lattices are similar and properly aligned. The periodicity of the superlattice, together with interlayer hybridization, may lead to a significant alteration in the band structure of the parent materials, giving rise to a plethora of interesting phenomena.[1,2] Graphene-based superlattices represent a particularly important class, serving as a versatile platform for the design and exploration of electronic systems characterized by intriguing physical properties.[1–3] The most extensively studied case within this category is the MS that forms when monolayer graphene (MLG) is deposited atop hBN, an atomically flat insulator with a hexagonal lattice nearly identical to that of graphene yet with a slightly larger crystal constant.[4–6] At the same time, its equally interesting counterpart based on BLG/hBN structure has received considerably less attention, even though it was this structure that initially unveiled the existence of magnetic minibands in the energy spectrum of moiré superlattices.[6] Recently, this system enabled the observation of fractional quantization within these minibands[7,8] and featured spontaneous polarization, giving rise to unconventional ferroelectricity[9,10] and the electronic ratchet effect[11] with mysterious origin. Furthermore, this system formed the foundation for the moiré synaptic transistor[12] highlighting the BLG-based MS as a peculiar platform drastically distinct from those made of MLG. Surprisingly, despite these experiments and theoretical analysis,[13–15] a comprehensive understanding of the BLG/hBN superlattice's electronic properties, especially of its remote energy bands, has been missing. The scarcity of experimental data highlights the challenges associated with fabricating perfectly aligned, low-disorder BLG/hBN moiré structures,[16] which are necessary to address this inquiry.

In this work, we produced such a high-quality perfectly aligned heterostructure and applied low-temperature magneto-transport measurements in combination with sub-THz excitation to get insights into the properties of this MS. We found that BLG/hBN alignment results in a series of compensated semimetals at some integer fillings of the moiré bands separated by van Hove singularities where Lifshitz transition converts electron Fermi pockets to those of hole type. A particularly pronounced semimetal emerges when 8 holes reside in the moiré unit cell, where coexisting electron and hole Fermi surfaces feature a giant magnetoresistance reaching 2350% at low magnetic field $B = 0.25$ T owing to intrinsically high carrier mobility. Next, by measuring the THz-driven Nernst effect in the remote bands, we observe giant valley splitting at $n/n_0 = -6$, pointing to a topological orbital magnetic moment characterized by an enhanced effective g_v-factor of 340. Last, using THz photoresistance measurements, we show that electron-electron umklapp processes are the dominant source of resistance in this system. Our results reveal the BLG/hBN MS as an interesting system in which to search for effects driven by interactions and topology.

Results

Device and measurement technique. Our sample is a BLG encapsulated between two slabs of hBN one of which was crystallographically aligned with BLG (Fig. 1a). The sample was patterned in the shape of a multi-terminal dual-gated field effect transistor (Fig. 1b) using standard nanofabrication techniques (See Methods). The top gate and source electrodes of this transistor were connected to a broadband antenna enabling incident THz radiation to funnel into the sample (Fig. 1b,c) akin to previous studies.[17,18] The sample was mounted in the chamber of the magneto-optical variable temperature (1.8-300 K, 7 T) cryostat (Quantum Design Opticool) and exposed to incident sub-terahertz radiation ($f_{\mathrm{THz}} = 0.14$ THz) through the system of lenses and mirrors.

To explore the electronic properties of our device, we simultaneously recorded longitudinal and transverse resistances: ρ_{xx} and ρ_{xy}, as well as measured THz photoresistance $\Delta\rho_{xx}^{\mathrm{THz}} = \rho_{xx}^{\mathrm{on}} - \rho_{xx}^{\mathrm{off}}$ (here *on* and *off* denote signals

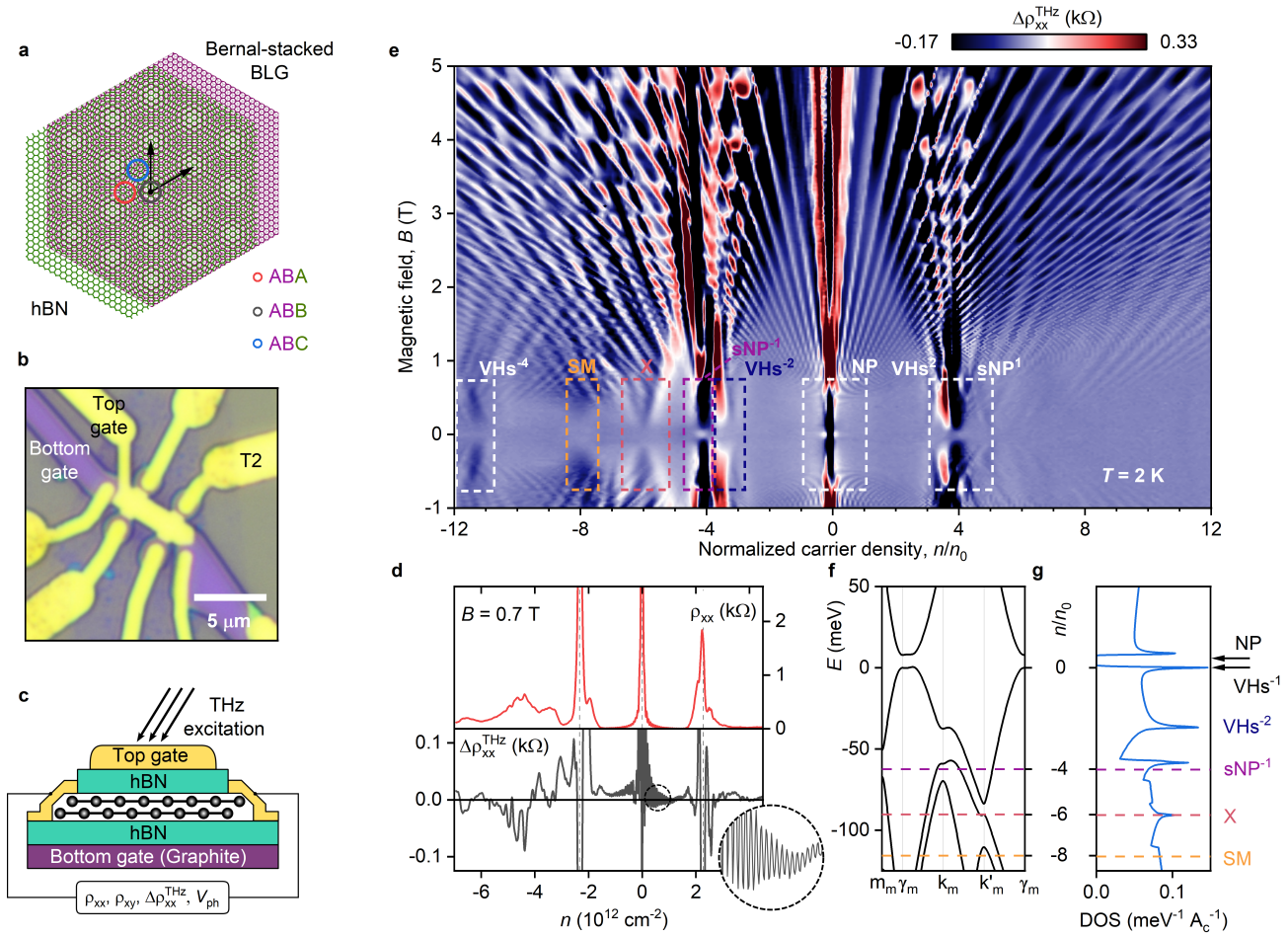

Figure 1. BLG/hBN moiré superlattice. a, Schematic of the moiré pattern formed between BLG and hBN. **b,** Optic image of the sample. The terahertz radiation is coupled to the structure via the top gate and the drain contacts. **c,** Schematic of the sample: BLG is encapsulated between two slabs of hBN only one of which was aligned with the BLG lattice. $\Delta\rho_{xx}^{THz}$ is measured in a four-terminal configuration using a low-noise double-modulation technique (Supporting Information). **d,** Comparison of $\rho_{xx}(n)$ and $\Delta\rho_{xx}^{THz}(n)$ at $B = 0.7$ T. Gray dashed lines indicate the positions of the main and secondary NPs. **e,** $\Delta\rho_{xx}^{THz}$ as a function of magnetic field and carrier density, measured at $T = 2$ K. The notation $4n_0 = 2.33 \cdot 10^{12}\text{cm}^{-2}$ refers to the single miniband's filling. **f-g,** Theoretical band structure and the DOS of the BLG/hBN superlattice calculated for the K high symmetry point of the original BLG BZ. Purple, red, and orange dashed lines mark the hole-side 1st sNP, 3rd VHs, and the semimetallic state respectively.

recorded in the dark and upon THz exposure), and the photovoltage, V_{ph}, built-up across the sample in response to incident radiation. While the photoresistance is a convenient probe for exploring quantization and scattering effects, as it isolates and highlights the contributions that are susceptible to changes in the electronic temperature, THz-induced V_{ph}, mainly governed by the thermoelectric response,[17,19,20] is highly sensitive to the changes of the Fermi surface topology, and thus can be used to probe effects occurring close to the Lifshitz transitions[21] making our method a convenient tool to probe various material properties on equal footing. See Supporting Information for details.

Sample characterization and Landau fan. Figure 1d shows the ρ_{xx} dependence on the gate-induced carrier density, n, measured at $B = 0.7$ T and reveals a standard superlattice behaviour. Namely, in addition to the central resistivity peak that appears at the main neutrality point (NP), two satellite peaks emerge

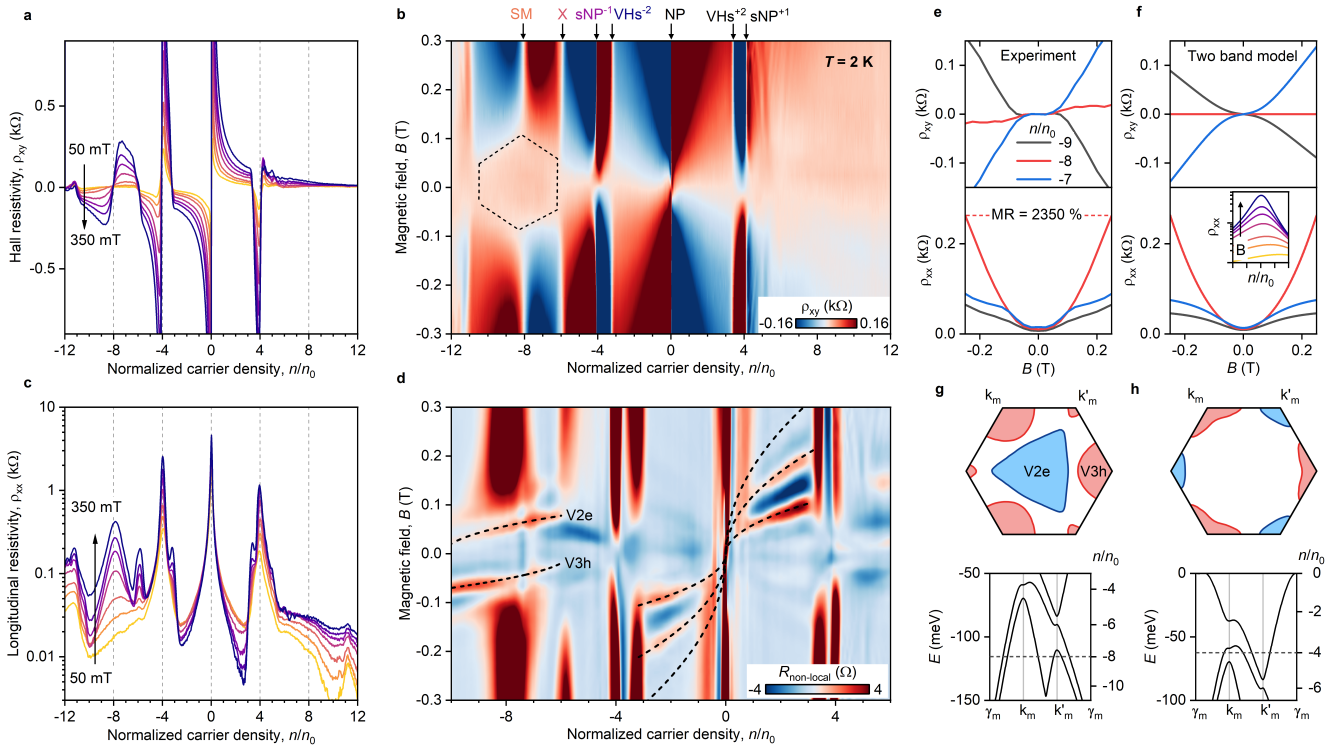

Figure 2. Low-field magnetotransport and compensated semimetals. a, Profiles of Hall ρ_{xy} vs n/n_0 for B-fields ranging from 50 mT (orange) to 350 mT (blue). **b,** Hall resistance ρ_{xy} mapped against B-field and the carrier densities **c,** Longitudinal resistance ρ_{xx} for B-fields ranging from 50 mT (orange) to 350 mT (blue). **d,** Non-local resistance map in a TMF configuration. Traces within the range of $-4 < n/n_0 < 4$ correspond to semi-classical orbits of carriers in the first pair of minibands. At higher negative fillings, traces marked as V2e and V3h reveal coexisting electron-like and hole-like Fermi surfaces. Results, presented in (a-d), were obtained at $T = 2$ K. **e-f,** Experimentally recorded $\rho_{xy}(B)$ and $\rho_{xx}(B)$ curves along with corresponding two-band conduction simulations near the compensation point. Carriers mobility of $\mu \sim 20$ m^2/Vs was obtained from fitting the experimental data. **g-h,** Hole-like (red) and electron-like (blue) Fermi-pockets in the mini-BZ of the compensated semimetallic states at $n/n_0 = -8$ and $n/n_0 = -4$, respectively.

at $4n_0 = \pm 2.33 \times 10^{12}$ cm^{-2} that is the density needed to fill the first superlattice miniband. Using this value, we estimate the superlattice period of $\lambda = 14.08$ nm and alignment angle of $\theta \approx 0°$. Figure 1d also plots the corresponding $\Delta\rho_{xx}^{THz}(n)$ dependence and reveales that while ρ_{xx} captures only dominant transport features at such a relatively small B, $\Delta\rho_{xx}^{THz}$ resolves pronounced quantum oscillations (See Supporting Information for details). For this reason, we proceed with the presentation of the Landau fan measured using the photoresistance technique.

Figure 1e maps the $\Delta\rho_{xx}^{THz}$ dependence on B and n/n_0. The Landau fan in Fig. 1e observed through $\Delta\rho_{xx}^{THz}$ reveals Landau quantization of the first miniband with filling factors $\nu = 4m, m = 1, 2, ...$, characteristic of the BLG bands, and resembles familiar Hofstader's butterfly at higher n.[6] In particular, close to both secondary NPs labeled as sNP^{-1} and sNP^{1}, the fan features the emergence of pronounced horizontal Hofstadter patterns upon increasing B. At $n/n_0 > 4$ and $B > 1.5$ T, we observe the continuation of the Landau quantization from the main band indicating the recovery of the unperturbed BLG electronic spectrum. At smaller B, we observe unusual low-frequency magnetooscillations with extrema that cannot be extrapolated to a single band filling at $B = 0$ T. These oscillations give rise to non-linear features on the Landau fan diagram. The origin of the latter

is unknown but recently similar features were attributed to the manifestation of the magnetic breakdown in MLG/hBN MS.[22] Alternative scenarios involve cyclotron gap closure due to inter-subband LL crossing in a multiband magnetotransport regime[23] and inter-subband scattering oscillations.[24,25] At $n/n_0 < -4$, the $\Delta\rho_{xx}^{THz}(n,B)$ pattern is much richer: in addition to the original structure of the BLG quantized spectrum, a mixed oscillation pattern is observed across the whole range $-12 < n/n_0 < -4$. Fast Fourier Transform (FFT) analysis reveals the presence of multiple fundamental frequencies with sophisticated dependencies on n, pointing to multi-band conduction (Supporting Information). However, this complexity makes it difficult to decipher the structure of the remote bands solely from the Landau fan diagram in Fig. 1e.

Nevertheless, low-field $\Delta\rho_{xx}^{THz}$ data can provide some hints, because the positive sign of $\Delta\rho_{xx}^{THz}$ can serve as an indicator of van Hove singularities (vHS). For example, at $n/n_0 = \pm 3.2$ THz-enhanced electron-hole scattering gives rise to increased resistance (see below) resulting in $\Delta\rho_{xx}^{THz} > 0$. This interpretation is also supported by standard Hall effect measurements, which show sign reversals in ρ_{xy} at this band filling (Fig. 2a,b and Supporting Figure S4). $\Delta\rho_{xx}^{THz}$, however, can provide some additional diagnostics as it reveals vHS (labeled as $vHS^{\pm 1}$) close to the main gap edge at $n/n_0 = \pm 0.2$ that is obscured by large Hall coefficient in the $\rho_{xy}(B)$ traces (Fig. 2a). Moreover, positive $\Delta\rho_{xx}^{THz}$ (marked as X in Fig. 1e) and the sign change of ρ_{xy} are also observed close to $n/n_0 = -6$ that point yet to another vHS^{-3}. The described sequence of vHS is in perfect agreement with the theoretical density of states (DOS) of the BLG/hBN MS band structure presented in Fig. 1f,g.

High-mobility compensated semimetals. For further analysis, we focus on the low-field magnetotransport measured in the dark. Figure 2c shows ρ_{xx} dependencies on n/n_0 and reveals familiar peaks at the main and secondary NPs. In addition, an unexpectedly prominent peak in ρ_{xx} emerges at $n/n_0 = -8$ when a small (~ 200 mT) magnetic field is applied. While this feature can be interpreted as the tertiary Dirac point,[26] our data refute this interpretation. Indeed, in the vicinity of $n/n_0 = -8$ there exists a wide range of n where ρ_{xy} is nearly zero for small B and increases nonlinearly when B is increased (dashed domain in Fig. 2b). Furthermore, the sign change of ρ_{xy} at $n/n_0 = -8$ is characterized by a relatively smooth transition with a finite slope, in contrast to the abrupt change observed at the main NP.

To understand these anomalies, we performed transverse magnetic focusing[27–29] (TMF) measurements (See Fig. 2d and Supporting Information) and revealed coexisting electron-type and hole-type resonances in the vicinity of $n/n_0 = -8$ (corresponding traces are labeled as V2e and V3h respectively, see Fig. 2d). The simultaneous appearance of electron-like and hole-like carriers implies the overlap of the minibands and the semimetallic nature of the observed state while the sign reversal of ρ_{xy} marks $n/n_0 = -8$ as its compensation point. Our conclusion is also corroborated by the two-band conduction model (Supporting Information) that captures both the $\rho_{xy}(B)$ evolution and the rapid growth of $\rho_{xx}(B)$ when passing through the compensation point (Fig. 2e,f).

Interestingly, at the compensation point, we observed large magnetoresistance ($MR = [\rho_{xx}(B) - \rho_{xx}(0)]/\rho_{xx}(0)$) reaching 2350 % already at 0.25 T somewhat larger than MR reported in some TMDC materials[30–32] at the same B and competitive to the MR recently observed in Dirac plasma.[33] Applying the two-band conduction model to the compensation point, where $MR = (\mu B)^2$, we obtain that such a large MR is enabled by intrinsically high carrier mobility of $\mu = 2 \times 10^5$ cm^2/Vs making BLG/hBN MS a promising candidate for searching effects driven by electron-hole interactions.

Last we note that the emergence of the semimetallic state at $n/n_0 = -8$ is in line with the theoretically calculated band structure that predicts the coexistence of large electron-like and hole-like Fermi pockets at this filling (Fig. 2g). Moreover, our calculations also suggest the presence of another compensated

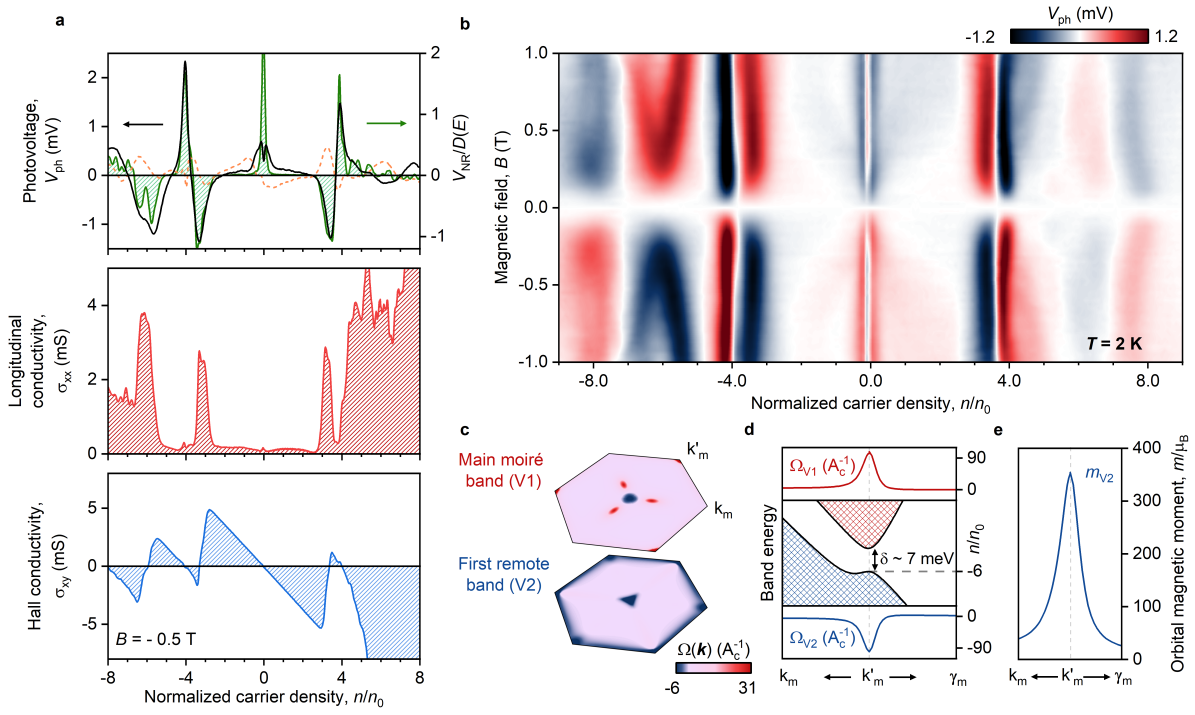

Figure 3. THz-driven Nernst effect and topological orbital magnetic moment. a, Components of $V_{\rm ph}$, symmetric (orange dashed line) and antisymmetric (black solid line) with respect to the $B-$field, plotted atop longitudinal conductivity $\sigma_{\rm xx}$ (red), and Hall conductivity $\sigma_{\rm xy}$ (blue). $B = -0.5$ T. The green line shows the expected Nernst photovoltage normalized to the DOS and calculated using eq. (1). **b,** Antisymmetric part of $V_{\rm ph}$ mapped against the $B-$field and n. A splitting of the vHs is observed at $n/n_0 = -6$, corresponding to the orbital magnetic moment of $\sim 170\mu_B$. **c,** Theoretically calculated Berry curvature $\Omega(\mathbf{k})$ distribution at the K-valley of the original BLG's BZ in the main and first remote hole-sided moiré bands showing the emergence of $\Omega(\mathbf{k})$ hot spots. **d,** Band structure and Berry curvature in the vicinity of the $k'_{\rm m}$-point of the mini-BZ around $n/n_0 = -6$. **e,** Topological orbital magnetic moment in the vicinity of $k'_{\rm m}$-point for the first remote band.

semimetallic state at $n/n_0 = -4$ yet with a smaller overlap between electron and hole bands (Fig. 2h).

Topological orbital magnetic moment. Thermoelectric response can provide additional information about the electronic properties of MS as it contains information on interaction effects or phenomena that emerge close to Lifshitz transitions.[34–37] The introduced THz technique allowed us to study the thermoelectric response of the BLG/hBN MS on equal footing with magnetotransport. To this end, we relied on the presence of thermoelectric contributions to the THz photovoltage.[17,19,20,38,39] When the magnetic field is applied, the thermoelectric photovoltage is dominated by the Nernst effect[40,41] in which

$$V_{\rm NR}/D(E) \propto \rho_{\rm xx}\frac{d\sigma_{\rm xy}}{dn} + \rho_{\rm xy}\frac{d\sigma_{\rm xx}}{dn}, \qquad (1)$$

where $D(E)$ is the DOS, $\sigma_{\rm xx}$ and $\sigma_{\rm xy}$ are the longitudinal and transverse elements of the conductivity tensor, respectively. Figure 3a shows that, indeed, the measured $V_{\rm ph}$ and $V_{\rm NR}$, calculated by eq. (1) using independently measured $\sigma_{\rm xx}$ and $\sigma_{\rm xy}$, are in good agreement with each other, signaling the dominance of the THz-driven Nernst effect in our experiments (Supporting Information).

Figure 3b shows the complete map of the antisymmetric-in-B part of $V_{\rm ph}$ across various fillings and magnetic fields. Among multiple peaks and dips in this plot, the feature near the

vHS at $n/n_0 = -6$ particularly stands out, as it exhibits a surprisingly strong splitting upon increasing magnetic field. To understand the origin of this anomaly, we return to the band structure (Fig. 3d) and notice a small gap between the main and the first remote bands at the $k'_{\rm m}$-point of the mini-Brillouin zone (BZ). While the first remote band is passing through a vHS at this point, the overlying main band edge resembles a gapped Dirac dispersion. The latter is intuitively expected to feature a strong Berry curvature $\Omega(\mathbf{k})$ hot spot and the associated orbital magnetic moment $m(\mathbf{k})$ that was indeed observed in our calculations shown in Fig. 3c-e (See Supporting Information). As the latter is opposite for the two parent valleys of the BLG bands, it is thus natural to attribute the splitting in Fig. 3b to the field-induced valley splitting with a greatly enhanced $g_{\rm v}$-factor.

By tracking the splitting value upon increasing B, one could estimate $g_{\rm v}-$factor through $\Delta E = 2mB = g_{\rm v}\mu_B B$ to be of the order of 340 and the orbital magnetic moment of $m = g_{\rm v}\mu_B/2 = 170\mu_B$, where μ_B is the Bohr magneton and ΔE is taken from Fig. 1g at corresponding fillings. In passing, we note that the thermoelectric Nernst effect measurements conducted in the remote band of the MLG/hBN superlattice revealed analogous valley splitting, corresponding to the $g_{\rm v}$-factor of ~ 130, several times smaller than in our sample.[36] Further comparison shows, that $g_{\rm v}$-factor, recorded in our BLG/hBN MS, is also several times larger than that observed at the main band edges of moire-free BLG[42,43] yet 3 times smaller than in the case of ABA trilayer graphene measured using sublattice-resolved scanning tunneling spectroscopy.[44]

High-T conductivity and umklapp scattering. Last, to complete the analysis of the electronic properties of the BLG/hBN MS, we reveal the scattering mechanisms that are responsible for the resistivity of such a system at elevated T. To this end, we firstly present the results of the conventional approach that relies on $\rho_{\rm xx}(T)$ measurements. Figure 4a shows $\rho_{\rm xx}(n)$ dependencies recorded at various sample temperatures. The data reveals an increase in the sample resistivity as T rises from 2.5 K to 200 K at all carrier densities except for the main NP. We observed a rapid surge in $\rho_{\rm xx}$ at $-4 < n/n_0 < 4$, contrasting a more gradual increase of $\rho_{\rm xx}$ in the remote bands. Figure 4b elaborates on this difference, showing the excess resistivity $\Delta\rho_{\rm xx}(T) = \rho_{\rm xx}(T) - \rho_{\rm xx}(2.5\ {\rm K})$ dependencies for various fillings. As we approach the midpoint of the first hole-side moire band, a clear T^2 growth with temperature is evident. However, a quadratic trend of $\Delta\rho_{\rm xx}(T)$ transitions to the linear behavior upon increasing n/n_0 passing through the filling at which $\Delta\rho_{\rm xx} \sim T^{3/2}$. At even higher negative fillings, $\Delta\rho_{\rm xx}(T)$ is relatively small and remains linearly dependent on temperature across the whole T-range (purple plot in Fig. 4b). In Supporting Information we provide further details of the $\Delta\rho_{\rm xx}(T)$ temperature dependence and its analysis.

While the linear-in-T contribution to $\rho_{\rm xx}(T)$ is commonly attributed to the electron-phonon scattering above the Bloch–Grüneisen temperature,[45] a T^2 scaling usually implies velocity-relaxing collisions among charge carriers.[46] The key difference in these contributions is that the former depends on the lattice temperature $T_{\rm L}$ whereas the latter on the electronic temperature, $T_{\rm e}$. In the conventional transport approach, the temperature of the sample sets both $T_{\rm L}$ and $T_{\rm e}$ making it nearly impossible to disentangle the dominant source of resistance from simple $\rho_{\rm xx}(T)$ fits especially when the T^α dependence with variable power α is observed.

THz photoresistance provides a convenient alternative to transport measurements, as the high-frequency radiation can selectively increase $T_{\rm e}$ while keeping the lattice cold (Supplementary Information). Indeed, in graphene-based MS this is possible because at cryogenic $T_{\rm L}$ the electronic system, characterized by a vanishing specific heat capacity, can be efficiently decoupled from the lattice.[47] In this context, $\Delta\rho_{\rm xx}^{\rm THz}$ serves as a complementary measure, as it extracts contributions sensitive only to the electronic temperature T_e. If $\Delta\rho_{\rm xx}^{\rm THz}$ were to be positive and finite in the metallic regime (*i.e.*, where $\rho_{\rm xx}$ grows with T), it would point to the presence of velocity-relaxing processes arising from inter-carrier collisions.

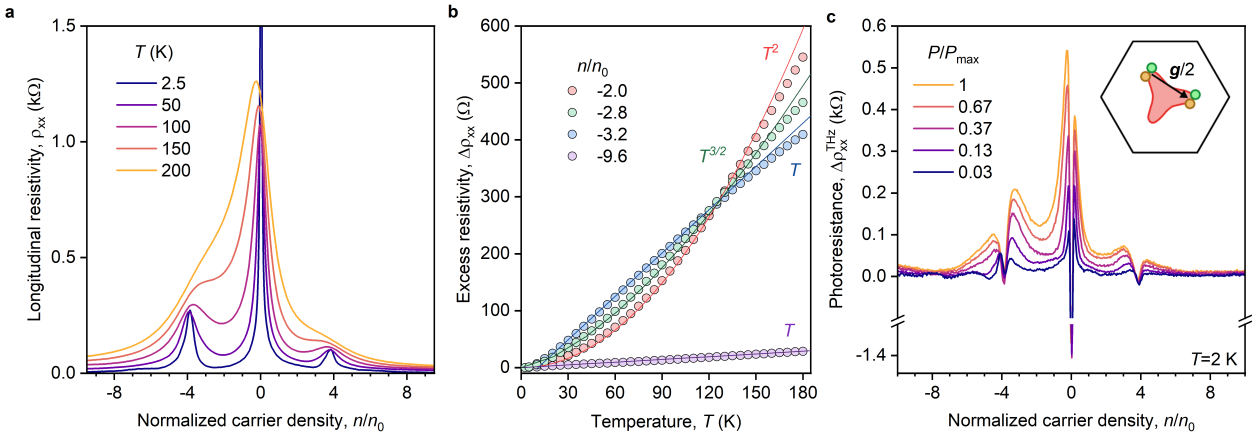

Figure 4. Umklapp scattering in the BLG/hBN moiré bands. a, Longitudinal resistivity ρ_{xx} vs n/n_0, measured at T varying from 2.5 K (blue) to 200 K (orange). **b,** Excess resistivity $\Delta\rho_{xx}$ as a function of T at various fillings, featuring a set of different functional behaviors T^{α} with α ranging from 1 to 2 depending on n/n_0. Fitted curves are plotted in the same color as the corresponding raw data. **c,** $\Delta\rho_{xx}^{\mathrm{THz}}$ as a function of n/n_0, measured upon varying incident THz powers, P. The sample was kept at fixed $T = T_{\mathrm{L}} = 2$ K. The inset illustrates the mechanism of umklapp scattering: after collisions, electrons appear on the opposite side of the Fermi surface so that the pair relaxes a reciprocal lattice unit vector $\boldsymbol{g}$.

Figure 4c presents $\Delta\rho_{xx}^{\mathrm{THz}}(n)$ curves at various incident 0.14 THz radiation powers P. For $-4 < n/n_0 < 4$, we observed large positive $\Delta\rho_{xx}^{\mathrm{THz}}$ that grows with increasing P (and, consequently, increasing T_e). Comparing it with the transport $\Delta\rho_{xx} \sim T^2$ scaling, it is natural to assign this positive $\Delta\rho_{xx}^{\mathrm{THz}}$ to the manifestation of umklapp scattering recently predicted to emerge in BLG MS.[48] Moreover, as $\Delta\rho_{xx}^{\mathrm{THz}}$ is also strong and positive upon approaching the vHS where both $\alpha = 1$ and 2 can be observed, we also conclude that in the main moiré band, the BLG/hBN MS is characterized by the interaction-limited conductivity. Last, the $\Delta\rho_{xx}^{\mathrm{THz}}(n)$ plots reveal that the impact of electron-electron scattering mechanisms is substantially suppressed for $|n/n_0| > 8$, consistent with weak linear-in-T $\Delta\rho_{xx}(T)$ dependence measured at these fillings pointing to the dominance of phonon scattering akin to the case of moiré-free MLG which has vanishing THz photoresistance (Supporting Information).

Conclusions

To sum up, we showed that a multi-messenger approach that combines standard magneto-transport techniques with low-energy sub-THz excitation can get deep insights into the properties of BLG/hBN MS. We demonstrated that BLG/hBN alignment results in the emergence of compensated semimetals at some integer fillings of the moiré bands separated by van Hove singularities where Lifshitz transition converts electron Fermi pockets to those of hole type. A particularly pronounced semimetal develops at $n/n_0 = -8$, where coexisting high-mobility electron and hole systems feature a giant magnetoresistance reaching 2350 % at a low magnetic field $B = 0.25$ T. Next, by measuring the THz-driven Nernst effect in remote bands, we observed a strong valley splitting that we attribute to the presence of a topological magnetic moment with a strongly enhanced effective g_{v}-factor of 340. Last, using THz photoresistance measurements, we show that the high-temperature conductivity of the BLG/hBN MS is limited by electron-electron umklapp processes in the main moire band which are suppressed in the remote bands. Our multi-faceted

analysis introduces THz-driven magnetotransport as an important tool to probe the electronic properties and interaction effects in vdW MS and uncovers BLG/hBN superlattices as an interesting system in which to search for effects governed by interactions and topology. It would be interesting to expand such studies to small-angle twisted bilayer graphene devices to get further insight into their properties.

Methods

Our sample was fabricated from Bernal-stacked BLG encapsulated by hBN slabs using a standard dry-transfer technique described elsewhere.[49] As an encapsulant, we used a large-area hBN flake that was unintentionally cracked into two pieces during exfoliation. One piece was aligned with respect to the BLG straight edge using an optical microscope equipped with micromanipulators and a high-precision rotation stage; this piece served as a top-gate dielectric. The second piece was intentionally misaligned by 30° with respect to the BLG and served as a bottom-gate dielectric. The use of a cracked hBN flake ensured that only one of the pieces forms a moiré superlattice with the BLG flake eliminating the possibility of a double-moiré structure formation.[50] We note, in passing, that similar structures were reported to exhibit unconventional ferroelectricity[9] - the latter was notably absent in our devices. The obtained heterostructure was released on a few-layer graphite strip serving as a back gate. We then used standard electron-beam lithography, selective reactive ion etching, and thin film metal deposition to pattern top and bottom gates and contact leads (Fig. 1b,c).

Associated content

Data availability statement

The data that support the findings of this study are available from the corresponding author upon reasonable request.

Supporting Information

Experimental setup, multi-messenger measurements, THz-driven photoresistance, THz-driven Nernst effect, carrier density extracted from the Hall effect, fast Fourier transform of the quantum oscillations, transverse magnetic focusing, two-band conduction model and magnetoresistance of compensated semimetal, further details of the resistivity temperature dependence, estimate of lattice overheating, photoresistance in monolayer graphene, calculation of band structure, calculation of orbital magnetic moment.

Notes

The authors declare no competing interests.
Pre-print is available.[51]
During the preparation of this manuscript we became aware of two related works.[52,53]

Acknowledgements

The research at NUS is supported by MOE Tier 2 (Award T2EP50123-0020, transport, and photoresistance measurements) and A*STAR under its Young Individual Research Grant (Award M22K3c0106, fabrication, photovoltage measurements). M.A.K. acknowledges the support of an internal funding program from the Center for Neurophysics and Neuromorphic Technologies. K.S.N. is grateful to the Ministry of Education, Singapore (Research Centre of Excellence award to the Institute for Functional Intelligent Materials, I-FIM, project No. EDUNC-33-18-279-V12) and to the Royal Society (UK, grant number RSRP\R\190000) for support. K.W. and T.T. acknowledge support from JSPS KAKENHI (grant nos. 20H00354, 21H05233 and 23H02052) and World Premier International Research Center Initiative (WPI), MEXT, Japan (hBN crystal synthesis and characterization). Z.Z. acknowledges support funding from the European Union's Horizon 2020 research and innovation programme under the Marie Skłodowska-Curie grant agreement No 101034431. IMDEA Nanoscience acknowledges support from the

"Severo Ochoa" Programme for Centres of Excellence in R&D (CEX2020-001039-S/AEI/10.13039/501100011033). P.P., Z.Z., and F.G. acknowledge support from NOVMOMAT, Grant PID2022-142162NB-I00 funded by MCIN/AEI/ 10.13039/501100011033 and by "ERDF A way of making Europe". S.S. and V.I.F. acknowledge support from the EC-FET Core 3 European Graphene Flagship Project, EC-FET Quantum Flagship Project 2D-SIPC, EPSRC Grants EP/S030719/1 and EP/V007033/1, and the Lloyd Register Foundation Nanotechnology Grant.

Author contributions

D.A.B. conceived the experiments, designed and supervised the research. A.L.S. conducted THz-driven and transport measurements with guidance from D.A.B. M.A.K., Y.W., and A.L.S. fabricated the devices. D.A.B., M.K., and A.K. developed a multi-messenger measurement system. P.P., Z.Z., and F.G. provided band structure calculations for BLG/hBN superlattices. S.S. and V.I.F. provided theory support on umklapp scattering. T.T. and K.W. grew hBN crystals. All authors contributed to the discussions.

References

(1) He, F.; Zhou, Y.; Ye, Z.; Cho, S.-H.; Jeong, J.; Meng, X.; Wang, Y. Moiré Patterns in 2D Materials: a Review. *ACS Nano* **2021**, *15*, 5944–5958.

(2) Andrei, E. Y.; MacDonald, A. H. Graphene Bilayers With a Twist. *Nature Materials* **2020**, *19*, 1265–1275.

(3) Wallbank, J. R.; Mucha-Kruczyński, M.; Chen, X.; Fal'ko, V. I. Moiré Superlattice Effects in Graphene/Boron-Nitride Van der Waals Heterostructures. *Annalen der Physik* **2015**, *527*, 359–376.

(4) Hunt, B.; Sanchez-Yamagishi, J. D.; Young, A. F.; Yankowitz, M.; LeRoy, B. J.; Watanabe, K.; Taniguchi, T.; Moon, P.; Koshino, M.; Jarillo-Herrero, P.; Ashoori, R. C. Massive Dirac Fermions and Hofstadter Butterfly in a Van der Waals Heterostructure. *Science* **2013**, *340*, 1427–1430.

(5) Ponomarenko, L. A. et al. Cloning of Dirac Fermions in Graphene Superlattices. *Nature* **2013**, *497*, 594–597.

(6) Dean, C. R.; Wang, L.; Maher, P.; Forsythe, C.; Ghahari, F.; Gao, Y.; Katoch, J.; Ishigami, M.; Moon, P.; Koshino, M.; Taniguchi, T.; Watanabe, K.; Shepard, K. L.; Hone, J.; Kim, P. Hofstadter's Butterfly and the Fractal Quantum Hall Effect in Moiré Superlattices. *Nature* **2013**, *497*, 598–602.

(7) Spanton, E. M.; Zibrov, A. A.; Zhou, H.; Taniguchi, T.; Watanabe, K.; Zaletel, M. P.; Young, A. F. Observation of Fractional Chern Insulators in a Van der Waals Heterostructure. *Science* **2018**, *360*, 62–66.

(8) Jeong, Y.; Park, H.; Kim, T.; Watanabe, K.; Taniguchi, T.; Jung, J.; Jang, J. Interplay of Valley, Layer and Band Topology Towards Interacting Quantum Phases in Bilayer Graphene Moiré Superlattice. 2023, 2310.05667. arXiv. https://arxiv.org/abs/2310.05667 (accessed March 16, 2024).

(9) Zheng, Z. et al. Unconventional Ferroelectricity in Moiré Heterostructures. *Nature* **2020**, *588*, 71–76.

(10) Niu, R. et al. Giant Ferroelectric Polarization in a Bilayer Graphene Heterostructure. *Nature Communications* **2022**, *13*, 6241.

(11) Zheng, Z. et al. Electronic Ratchet Effect in a Moiré System: Signatures of Excitonic Ferroelectricity. 2023, 2306.03922. arXiv. https://arxiv.org/abs/2306.03922 (accessed March 16, 2024).

(12) Yan, X.; Zheng, Z.; Sangwan, V. K.; Qian, J. H.; Wang, X.; Liu, S. E.; Watanabe, K.; Taniguchi, T.; Xu, S.-Y.; Jarillo-Herrero, P.; Ma, Q.; Hersam, M. C. Moiré Synaptic Transistor with Room-Temperature Neuromorphic Functionality. *Nature* **2023**, *624*, 551–556.

(13) Chen, X.; Wallbank, J. R.; Mucha-Kruczyński, M.; McCann, E.; Fal'ko, V. I. Zero-Energy Modes and Valley Asymmetry in the Hofstadter Spectrum of Bilayer Graphene Van der Waals Heterostructures With hBN. *Phys. Rev. B* **2016**, *94*, 045442.

(14) Moon, P.; Koshino, M. Electronic Properties of Graphene/Hexagonal-Boron-Nitride Moiré Superlattice. *Phys. Rev. B* **2014**, *90*, 155406.

(15) Pantaleón, P. A.; Cea, T.; Brown, R.; Walet, N. R.; Guinea, F. Narrow Bands, Electrostatic Interactions and Band Topology in Graphene Stacks. *2D Materials* **2021**, *8*, 044006.

(16) Endo, K.; Komatsu, K.; Iwasaki, T.; Watanabe, E.; Tsuya, D.; Watanabe, K.; Taniguchi, T.; Noguchi, Y.; Wakayama, Y.; Morita, Y.; Moriyama, S. Topological Valley Currents in Bilayer Graphene/Hexagonal Boron Nitride Superlattices. *Applied Physics Letters* **2019**, *114*, 243105.

(17) Bandurin, D. A.; Gayduchenko, I.; Cao, Y.; Moskotin, M.; Principi, A.; Grigorieva, I. V.; Goltsman, G.; Fedorov, G.; Svintsov, D. Dual Origin of Room Temperature Sub-Terahertz Photoresponse in Graphene Field Effect Transistors. *Applied Physics Letters* **2018**, *112*, 141101.

(18) Bandurin, D. A. et al. Resonant Terahertz Detection Using Graphene Plasmons. *Nature Communications* **2018**, *9*, 5392.

(19) Cai, X.; Sushkov, A. B.; Suess, R. J.; Jadidi, M. M.; Jenkins, G. S.; Nyakiti, L. O.; Myers-Ward, R. L.; Li, S.; Yan, J.; Gaskill, D. K.; Murphy, T. E.; Drew, H. D.; Fuhrer, M. S. Sensitive Room-Temperature Terahertz Detection Via the Photothermoelectric Effect in Graphene. *Nature Nanotechnology* **2014**, *9*, 814–819.

(20) Castilla, S.; Terrés, B.; Autore, M.; Viti, L.; Li, J.; Nikitin, A. Y.; Vangelidis, I.; Watanabe, K.; Taniguchi, T.; Lidorikis, E.; Vitiello, M. S.; Hillenbrand, R.; Tielrooij, K.-J.; Koppens, F. H. Fast and Sensitive Terahertz Detection Using an Antenna-Integrated Graphene pn Junction. *Nano Letters* **2019**, *19*, 2765–2773.

(21) Abrikosov, A. Fundamentals of the Theory of Metals; Courier Dover Publications, 2017.

(22) Moon, P.; Kim, Y.; Koshino, M.; Taniguchi, T.; Watanabe, K.; Smet, J. H. Non-Linear Landau Fan Diagram for Graphene Electrons Exposed to a Moiré Potential. 2023, 2311.16412. https://arxiv.org/abs/2311.16412 (accessed March 16, 2024).

(23) Lu, X. et al. High-Order Minibands and Interband Landau Level Reconstruction in Graphene Moiré Superlattices. *Phys. Rev. B* **2020**, *102*, 045409.

(24) Phinney, I. Y.; Bandurin, D. A.; Collignon, C.; Dmitriev, I. A.; Taniguchi, T.; Watanabe, K.; Jarillo-Herrero, P. Strong Interminivalley Scattering in Twisted Bilayer Graphene Revealed by High-Temperature Magneto-Oscillations. *Phys. Rev. Lett.* **2021**, *127*, 056802.

(25) Tomić, P.; Rickhaus, P.; Garcia-Ruiz, A.; Zheng, G.; Portolés, E.; Fal'ko, V.; Watanabe, K.; Taniguchi, T.; Ensslin, K.; Ihn, T.; de Vries, F. K. Scattering Between Minivalleys in Twisted Double Bilayer Graphene. *Phys. Rev. Lett.* **2022**, *128*, 057702.

(26) Chen, G.; Sui, M.; Wang, D.; Wang, S.; Jung, J.; Moon, P.; Adam, S.; Watanabe, K.; Taniguchi, T.; Zhou, S.; Koshino, M.; Zhang, G.; Zhang, Y. Emergence of Tertiary Dirac Points in Graphene Moiré Superlattices. *Nano Letters* **2017**, *17*, 3576–3581.

(27) Tsoi, V. Focusing of Electrons in a Metal by a Transverse Magnetic Field. *ZhETF Pisma Redaktsiiu* **1974**, *19*, 114.

(28) Taychatanapat, T.; Watanabe, K.; Taniguchi, T.; Jarillo-Herrero, P. Electrically Tunable Transverse Magnetic Focusing in Graphene. *Nature Physics* **2013**, *9*, 225–229.

(29) Lee, M.; Wallbank, J. R.; Gallagher, P.; Watanabe, K.; Taniguchi, T.; Fal'ko, V. I.; Goldhaber-Gordon, D. Ballistic Miniband Conduction in a Graphene Superlattice. *Science* **2016**, *353*, 1526–1529.

(30) Ali, M. N.; Xiong, J.; Flynn, S.; Tao, J.; Gibson, Q. D.; Schoop, L. M.; Liang, T.; Haldolaarachchige, N.; Hirschberger, M.; Ong, N. P.; Cava, R. J. Large, Non-Saturating Magnetoresistance in WTe_2. *Nature* **2014**, *514*, 205–208.

(31) Keum, D. H.; Cho, S.; Kim, J. H.; Choe, D.-H.; Sung, H.-J.; Kan, M.; Kang, H.; Hwang, J.-Y.; Kim, S. W.; Yang, H.; Chang, K. J.; Lee, Y. H. Bandgap Opening in Few-Layered Monoclinic $MoTe_2$. *Nature Physics* **2015**, *11*, 482–486.

(32) Mangelsen, S.; Naumov, P. G.; Barkalov, O. I.; Medvedev, S. A.; Schnelle, W.; Bobnar, M.; Mankovsky, S.; Polesya, S.; Näther, C.; Ebert, H.; Bensch, W. Large Nonsaturating Magnetoresistance and Pressure-Induced Phase Transition in the Layered Semimetal $HfTe_2$. *Phys. Rev. B* **2017**, *96*, 205148.

(33) Xin, N.; Lourembam, J.; Kumaravadivel, P.; Kazantsev, A. E.; Wu, Z.; Mullan, C.; Barrier, J.; Geim, A. A.; Grigorieva, I. V.; Mishchenko, A.; Principi, A.; Fal'ko, V. I.; Ponomarenko, L. A.; Geim, A. K.; Berdyugin, A. I. Giant Magnetoresistance of Dirac Plasma in High-Mobility Graphene. *Nature* **2023**, *616*, 270–274.

(34) Ghawri, B.; Mahapatra, P. S.; Garg, M.; Mandal, S.; Bhowmik, S.; Jayaraman, A.; Soni, R.; Watanabe, K.; Taniguchi, T.; Krishnamurthy, H. R.; Jain, M.; Banerjee, S.; Chandni, U.; Ghosh, A. Breakdown of Semiclassical Description of Thermoelectricity in Near-Magic Angle Twisted Bilayer Graphene. *Nature Communications* **2022**, *13*, 1522.

(35) Guarochico-Moreira, V. H.; Anderson, C. R.; Fal'ko, V.; Grigorieva, I. V.; Tóvári, E.; Hamer, M.; Gorbachev, R.; Liu, S.; Edgar, J. H.; Principi, A.; Kretinin, A. V.; Vera-Marun, I. J. Thermopower in hBN/Graphene/hBN Superlattices. *Phys. Rev. B* **2023**, *108*, 115418.

(36) Moriya, R.; Kinoshita, K.; Crosse, J. A.; Watanabe, K.; Taniguchi, T.; Masubuchi, S.; Moon, P.; Koshino, M.; Machida, T. Emergence of Orbital Angular Moment at van Hove Singularity in Graphene/h-BN Moiré Superlattice. *Nature Communications* **2020**, *11*, 5380.

(37) Paul, A. K.; Ghosh, A.; Chakraborty, S.; Roy, U.; Dutta, R.; Watanabe, K.; Taniguchi, T.; Panda, A.; Agarwala, A.; Mukerjee, S.; Banerjee, S.; Das, A. Interaction-Driven Giant Thermopower in Magic-Angle Twisted Bilayer Graphene. *Nature Physics* **2022**, *18*, 691–698.

(38) Otteneder, M.; Hubmann, S.; Lu, X.; Kozlov, D. A.; Golub, L. E.; Watanabe, K.; Taniguchi, T.; Efetov, D. K.; Ganichev, S. D. Terahertz Photogalvanics in Twisted Bilayer Graphene Close to the Second Magic Angle. *Nano Letters* **2020**, *20*, 7152–7158.

(39) Principi, A.; Bandurin, D.; Rostami, H.; Polini, M. Pseudo-Euler Equations From Nonlinear Optics: Plasmon-Assisted Photodetection Beyond Hydrodynamics. *Phys. Rev. B* **2019**, *99*, 075410.

(40) Cao, H.; Aivazian, G.; Fei, Z.; Ross, J.; Cobden, D. H.; Xu, X. Photo-Nernst Current in Graphene. *Nature Physics* **2016**, *12*, 236–239.

(41) Wu, S.; Wang, L.; Lai, Y.; Shan, W.-Y.; Aivazian, G.; Zhang, X.; Taniguchi, T.; Watanabe, K.; Xiao, D.; Dean, C.; Hone, J.; Li, Z.; Xu, X. Multiple Hot-Carrier Collection in Photo-excited Graphene Moiré Superlattices. *Science Advances* **2016**, *2*, e1600002.

(42) Overweg, H.; Knothe, A.; Fabian, T.; Linhart, L.; Rickhaus, P.; Wernli, L.; Watanabe, K.; Taniguchi, T.; Sánchez, D.; Burgdörfer, J.; Libisch, F.; Fal'ko, V. I.; Ensslin, K.; Ihn, T. Topologically Nontrivial Valley States in Bilayer Graphene Quantum Point Contacts. *Phys. Rev. Lett.* **2018**, *121*, 257702.

(43) Lee, Y.; Knothe, A.; Overweg, H.; Eich, M.; Gold, C.; Kurzmann, A.; Klasovika, V.; Taniguchi, T.; Wantanabe, K.; Fal'ko, V.; Ihn, T.; Ensslin, K.; Rickhaus, P. Tunable Valley Splitting Due to Topological Orbital Magnetic Moment in Bilayer Graphene Quantum Point Contacts. *Phys. Rev. Lett.* **2020**, *124*, 126802.

(44) Ge, Z.; Slizovskiy, S.; Joucken, F.; Quezada, E. A.; Taniguchi, T.; Watanabe, K.; Fal'ko, V. I.; Velasco, J. Control of Giant Topological Magnetic Moment and Valley Splitting in Trilayer Graphene. *Phys. Rev. Lett.* **2021**, *127*, 136402.

(45) Efetov, D. K.; Kim, P. Controlling Electron-Phonon Interactions in Graphene at Ultrahigh Carrier Densities. *Phys. Rev. Lett.* **2010**, *105*, 256805.

(46) Wallbank, J. R.; Krishna Kumar, R.; Holwill, M.; Wang, Z.; Auton, G. H.; Birkbeck, J.; Mishchenko, A.; Ponomarenko, L. A.; Watanabe, K.; Taniguchi, T.; Novoselov, K. S.; Aleiner, I. L.; Geim, A. K.; Fal'ko, V. I. Excess Resistivity in Graphene Superlattices Caused by Umklapp Electron–Electron Scattering. *Nature Physics* **2019**, *15*, 32–36.

(47) Aamir, M. A.; Moore, J. N.; Lu, X.; Seifert, P.; Englund, D.; Fong, K. C.; Efetov, D. K. Ultrasensitive Calorimetric Measurements of the Electronic Heat Capacity of Graphene. *Nano Letters* **2021**, *21*, 5330–5337.

(48) Moulsdale, C.; Fal'ko, V. Umklapp Electron-Electron Scattering in Bilayer Graphene Moiré Superlattice. *Phys. Rev. B* **2023**, *107*, 144111.

(49) Purdie, D. G.; Pugno, N. M.; Taniguchi, T.; Watanabe, K.; Ferrari, A. C.; Lombardo, A. Cleaning Interfaces in Layered Materials Heterostructures. *Nature Communications* **2018**, *9*, 5387.

(50) Wang, Z. et al. Composite Super-Moiré Lattices in Double-Aligned Graphene Heterostructures. *Science Advances* **2019**, *5*, eaay8897.

(51) Shilov, A. L.; Kashchenko, M. A.; Pantaleón, P. A.; Kravtsov, M.; Kudriashov, A.; Zhan, Z.; Taniguchi, T.; Watanabe, K.; Slizovskiy, S.; Novoselov, K. S.; Fal'ko, V. I.; Guinea, F.; Bandurin, D. A. High-mobility compensated semimetals, orbital magnetization, and umklapp scattering in bilayer graphene moiré superlattices. 2023, 2311.05124. arXiv. https://arxiv.org/abs/2311.05124 (accessed March 16, 2024).

(52) Bocarsly, M.; Uzan, M.; Roy, I.; Grover, S.; Xiao, J.; Dong, Z.; Labendik, M.; Uri, A.; Huber, M. E.; Myasoedov, Y.; Watanabe, K.; Taniguchi, T.; Yan, B.; Levitov, L. S.; Zeldov, E. De Haas–Van Alphen Spectroscopy and

Magnetic Breakdown in Moiré Graphene. *Science* **2024**, *383*, 42–48.

(53) Jat, M. K.; Mishra, S.; Mann, H. K.; Bajaj, R.; Watanabe, K.; Taniguchi, T.; Krishnamurthy, H. R.; Jain, M.; Bid, A. Controlling Umklapp Scattering in a Bilayer Graphene Moiré Superlattice. *Nano Letters* **2024**, *24*, 2203–2209.